Available online at www.sciencedirect.com
SCIENCE DIRECT®
Combustion and Flame 142 (2005) 329–347
Combustion and Flame
www.elsevier.com/locate/combustflame

Large-eddy simulation of a bluff-body-stabilized non-premixed flame using a recursive filter-refinement procedure

Venkatramanan Raman *, Heinz Pitsch

Center for Turbulence Research, Stanford University, Stanford, CA 94305, USA

Received 7 July 2004; received in revised form 3 March 2005; accepted 9 March 2005

Available online 3 May 2005

Abstract

A large-eddy simulation (LES) of a bluff-body-stabilized flame has been carried out using a new strategy for LES grid generation. The recursive filter-refinement procedure (RFRP) has been used to generate optimized clustering for variable density combustion simulations. A methane–hydrogen fuel-based bluff-body-stabilized experimental configuration has been simulated using state-of-the-art LES algorithms and subfilter models. The combustion chemistry is described using a precomputed, laminar flamelet model-based look-up table. The GRI-2.11 mechanism is used to build the look-up table parameterized by mixture fraction and scalar dissipation rate. A beta function is used for the subfilter mixture fraction filtered density function (FDF). The simulations show good agreement with experimental data for the velocity field. Time-averaged profiles of major species and temperature are very well reproduced by the simulation. The mixture fraction profiles show excellent agreement at all locations, which helps in understanding the validity of flamelet assumption for this flame. The results indicate that LES computations are able to quantitatively predict the flame structure quite accurately using the laminar flamelet model. Simulations tend to corroborate experimental evidence that local extinction is not significant for this flame.
© 2005 The Combustion Institute. Published by Elsevier Inc. All rights reserved.

Keywords: Large-eddy simulation; Combustion; Flamelet model; Recursive filter refinement; Bluff-body-stabilized flow

1. Introduction

Turbulent reacting flows form an important class of industrially relevant systems that are amenable to numerical simulations. With increased importance of pollutant control and process optimization, computational fluid dynamics (CFD) can play a vital role in the design and development of environment-friendly chemical processes [1]. In particular, combusting flows comprise wide variety of applications including aircraft engines, power production, and chemical product synthesis [2]. As many of these processes involve complex interaction of turbulence and reaction, CFD techniques need to contain sufficient description of the flow as well as reaction physics. In low-Mach-number flows, reactions affect the flow indirectly through the change in density that occurs with heat release [3]. This facilitates independent development of flow and reaction models. In the context of such hybrid solvers, the large-eddy simulation (LES) methodology has emerged as the choice of numerical technique for handling turbulent reactive flows [4].

* Corresponding author.
E-mail address: vraman@stanford.edu (V. Raman).

0010-2180/$ – see front matter © 2005 The Combustion Institute. Published by Elsevier Inc. All rights reserved.
doi:10.1016/j.combustflame.2005.03.014

Combustion models for LES are usually derived from the corresponding RANS models. Because LES resolves the large-scale structures, subfilter model contribution is typically smaller in LES than in RANS methods. Nevertheless, reactive flow still poses a computational challenge, as the interaction of flow and chemistry typical of combustion occurs at length scales much smaller than the LES filter width.

Eulerian transport equations of reactive scalars cannot be solved directly due to the unclosed chemical source term [5]. In Eulerian techniques like LES, all subgrid quantities need to be modeled. Due to the fast chemical time scales in combustion processes, reactions may occur exclusively at subfilter scales [2]. Interestingly fast chemistry also ensures that the multidimensional solution space reduces to a low-dimensional manifold [6]. In general, reaction models evolve the solution vector in terms of a reduced number of tracking scalars. The steady laminar flamelet model [6] uses mixture fraction and scalar dissipation rate to model chemical reactions. First-order conditional moment closure (CMC) defines transport equations for the conditional means of the species conditioned on the mixture fraction [7,8]. For chemically reacting systems with slower time scales, the mixture fraction (and scalar dissipation rate) alone cannot describe the distributed reaction regime [2,9], and the use of additional scalars may be required. In systems with negligible local extinction, the flamelet model has been shown to be quite accurate [3,10].

LES methods have thus advanced from an academic tool to a practical technique for studying complex flow physics. Such flows comprise a range of computational and modeling challenges. One of the important characteristics of such complex burners is the recirculation zone that helps stabilize the flame and prevent extinction. As combustors are closed systems, the interaction of the flame with the walls should be modeled appropriately. In addition, the effect of the inflow geometry, especially the mixing in the shear layer separating the inflow jet from the recirculation zone, needs to be captured accurately. It has been observed [11] that such flows are highly transient as well as three-dimensional and cannot be captured by RANS or two-dimensional calculations.

One of the purposes of the current work is to establish the relative superiority of LES-based modeling of such complex reacting flows. Though LES simulations cannot resolve the reaction length scales, it will be shown that the prediction of large-scale scalar mixing combined with the unsteady formulation is vital to quantitative prediction of reacting flows. For this purpose, the methane–hydrogen fuel-based bluff-body-stabilized flame studied experimentally at the University of Sydney and at Sandia National Laboratories was chosen [12]. This flow configuration corresponds to that of practical systems with large recirculation zones keeping the reaction zone attached. It is essential for any turbulence model to capture the complex flow structure to describe the flame physics accurately. The flame is stabilized by recirculation zones near the solid bluff body, with strong turbulent mixing initiating and maintaining the reactions. The experimental measurements provide both velocity and scalar fields obtained as radial profiles at select axial locations. The velocity measurements are carried out under flow conditions slightly different from those for the scalar measurements [12]. This experiment forms the base case of a series of data sets obtained using various fuel inflow velocities [12]. It has been noted that this particular flame does not exhibit significant extinction, indicating that a laminar flamelet-type approximation could be adequate in capturing the species profiles, once the scalar mixing process is correctly predicted.

Several simulations of this flow configuration have been carried out in the past, using primarily RANS- and PDF-based approaches [13–17] to describe the velocity field. A detailed comparison of the simulation results has been carried out elsewhere [18]. All of these simulations use flamelet, CMC, or equilibrium chemistry assumptions to model reactions. The RANS-based simulations [13,15] show reasonable agreement in the near-bluff body region but deviate significantly at the downstream locations. PDF-based simulations [16] show reasonably good agreement for the conserved scalar profiles, but no detailed comparisons with other species were discussed. It is noted that all RANS simulations were carried out using first-order gradient diffusion-based closures for the turbulent scalar flux, while the joint velocity–scalar PDF methods inherently contain a second-order formulation similar to the Reynolds stress models [19]. As LES simulations involve spatial filtering, in a well-resolved computation, the locally isotropic gradient diffusion hypotheses should have a smaller effect on the scalar profiles. The superior formulation for the momentum equations should lead to better reproduction of the velocity profiles. In addition, Masri and co-workers [12,17] have reported significant vortex shedding at the edge of the bluff body, which can be captured only through a three-dimensional transient simulation. We show that the LES computations, compared with ensemble averaged turbulence models such as RANS and PDF methods, provide largely improved results in applications to chemically reacting flows. It is demonstrated that the scalar mixing and turbulence are well predicted, implying that the complex dynamics of the flame are captured accurately.

In Section 2, the mathematical models and the recursive filter-refinement procedure (RFRP) based on scalar variance used in the simulation are discussed.

Section 3 details the numerical algorithms, and Section 4 discusses the results and the comparison with the experimental data.

2. Mathematical models

2.1. Governing equations

For variable density flows, a Favre-filtered variable is defined as

$$\tilde{f} = \frac{1}{\bar{\rho}} \int \rho f \mathbf{G}(\mathbf{x}, \mathbf{y})\, d\mathbf{y}, \tag{1}$$

where $\bar{\rho}$ is the filtered density field and $\mathbf{G}(\mathbf{x}, \mathbf{y})$ is a three-dimensional spatial filter. The filtered continuity and momentum equations can then be written as

$$\frac{\partial \bar{\rho}}{\partial t} + \frac{\partial \bar{\rho}\tilde{u}_i}{\partial x_i} = 0, \tag{2}$$

$$\frac{\partial \bar{\rho}\tilde{u}_i}{\partial t} + \frac{\partial \bar{\rho}\tilde{u}_i\tilde{u}_j}{\partial x_j} = -\frac{\partial \tilde{P}}{\partial x_i} + \frac{\partial \tau_{ij}}{\partial x_j} + \frac{\partial T_{ij}}{\partial x_j}, \tag{3}$$

where τ_{ij} is the viscous stress tensor given by

$$\tau_{ij} = \mu\left(\frac{\partial \tilde{u}_i}{\partial x_j} + \frac{\partial \tilde{u}_j}{\partial x_i} - \frac{2}{3}\frac{\partial \tilde{u}_k}{\partial x_k}\delta_{ij}\right) = 2\mu\tilde{S}_{ij}, \tag{4}$$

and $T_{ij} = \bar{\rho}\tilde{u}_i\tilde{u}_j - \bar{\rho}\widetilde{u_i u_j}$ denotes the subfilter stresses. The transport equation for the conserved scalar can be written as

$$\frac{\partial \bar{\rho}\tilde{Z}}{\partial t} + \frac{\partial \bar{\rho}\tilde{u}_j\tilde{Z}}{\partial x_j} = \frac{\partial}{\partial x_j}\left(\bar{\rho}\tilde{D}\frac{\partial \tilde{Z}}{\partial x_j}\right) + \frac{\partial M}{\partial x_j}, \tag{5}$$

where $M = \bar{\rho}\widetilde{u_i Z} - \bar{\rho}\tilde{u}_i\tilde{Z}$. Both T_{ij} and M should require closure models. Several models have been proposed [20,21]. Most commonly used are the gradient diffusion hypothesis-based models [20,22]. The subfilter stress is then modeled using

$$T_{ij} = 2\mu_t S_{ij}. \tag{6}$$

The eddy viscosity μ_t is obtained using the Smagorinsky model [20] as

$$\mu_t = C_s\bar{\rho}\Delta^2\mathcal{S}, \tag{7}$$

where $\mathcal{S}$ is the magnitude of the strain rate and Δ is the characteristic width of the filter. The coefficient C_s is determined using a dynamic procedure [23,24]. The dynamic model used here [23] assumes spatial homogeneity in the azimuthal direction. Even though this assumption is not strictly valid in the present case, the high computational cost of localized formulations [24] makes the use of this assumption attractive. It is expected that a well-resolved grid will be able to minimize the small errors that might result from this assumption.

The subfilter scalar flux is also modeled using a gradient diffusion hypothesis as

$$M = \Gamma_t\frac{\partial \tilde{Z}}{\partial x_j}, \tag{8}$$

where Γ_t is the eddy diffusivity. The eddy diffusivity is computed using a formulation similar to the eddy viscosity

$$\Gamma_t = C_z\bar{\rho}\Delta^2\mathcal{S}, \tag{9}$$

where C_z is determined dynamically [23]. It is apparent that the eddy viscosity and diffusivity are modeled using the same functional form and differ only in the coefficients [25]. The ratio C_z/C_s then gives the turbulent Schmidt number.

The models specified above along with the scalar transport equation (Eq. (5)) are used to obtain the filtered mixture fraction. Because the filter widths are much larger than the Kolmogorov (or Batchelor) scales, the unresolved mixture fraction variations cannot be neglected. Hence, models need to be formulated to quantify the subfilter fluctuations. Usually, the filtered mixture fraction along with the subfilter variance is used to define a probability density function that represents the statistics of the subfilter scalar fluctuations. DNS studies have shown that the PDF of a binary scalar mixing can be represented by a beta function parameterized by the mean and the variance [26,27]. Also in the context of LES, Jimenez et al. [28] have shown that the subfilter PDF of a conserved scalar in homogeneous isotropic turbulence can be approximated by a beta function.

To estimate the subfilter variance, a local equilibrium assumption that neglects all transport in physical space is used [29]. The model for the variance can then be written as

$$\widetilde{Z''^2} = C_v\Delta^2(\nabla\tilde{Z})^2, \tag{10}$$

where C_v is determined using a dynamic model [30]. It is noted that despite the wide use of the local equilibrium assumption, the above dynamic model can be inaccurate in general flows [31–33]. One of the main issues is that the local equilibrium assumption is not strictly valid in inhomogeneous flows, which can lead to an underprediction of the subfilter variance. In addition, scalar fields exhibit large-scale instantaneous spatial inhomogeneities in a bluff body flow, and the dynamic formulation with azimuthal averaging could lead to additional errors. Ideally, a transport equation for the subfilter variance should be used [31]. Then the filtered scalar dissipation requires detailed modeling, and no satisfactory model has been formulated yet. The next section details a methodology to decrease the impact of subfilter models.

2.2. Recursive filter-refinement procedure

One of the key issues in LES simulations with implicit filtering is the lack of a grid independence criterion due to the implicit dependence of the filter width on the local mesh. To exhibit a true grid-independent LES simulation, a series of computations should be performed with the same mesh but varying filter widths, as well as a fixed filter width and varying mesh size. Such a strategy is computationally infeasible due to the high computational cost of LES simulations. A practical strategy to minimize grid-based errors is to carry out an adaptive mesh refinement based on a measure of the subfilter resolution. For example, the RMS velocity fluctuations can be compared with the modeled subfilter velocity fluctuation to obtain an estimate of the fraction of the turbulent energy resolved. However, this would require time averaging over a large number of iterations to reduce statistical fluctuations and may not be feasible in highly unsteady flows. Here, we propose a simpler yet consistent scheme with the aim of resolving the scalar energy. Such a refinement is important not only for ensuring grid independence but also for measuring general grid quality. In non-premixed combustion, the LES solution is extremely sensitive to scalar resolution, and the scalar field is much more sensitive to grid quality than the velocity field. This implies that a measure of the scalar energy resolution is a good indicator of grid quality.

The current strategy relies on simulations with successively increased resolution. For this purpose, first, a cold flow solution with reasonably fine mesh is obtained. This solution is then interpolated to a coarse mesh without any grid clustering. The variable density simulation is then started and continued for a few hundred time steps. At this stage a refinement strategy is proposed as follows. The subfilter variance field as a fraction of the maximum subfilter variance is evaluated.

$$\epsilon = \frac{\widetilde{Z''^2}}{\tilde{Z}(1-\tilde{Z})}, \tag{11}$$

where it can be easily shown that $\widetilde{Z''^2}_{\max} = \tilde{Z}(1-\tilde{Z})$ for any given $\tilde{Z}$. A simple relation between fractional scalar energy and filter width is formulated from scaling laws as follows. As the actual turbulent dissipation and scalar dissipation do not change with filter width, provided the filter width is located in the inertial range, the following relations in terms of this invariant quantities can be used:

$$\tilde{\chi} \propto \frac{u'}{\Delta}\widetilde{Z''^2}, \tag{12}$$

$$\tilde{\varepsilon} \propto \frac{u'^3}{\Delta}. \tag{13}$$

Where, $\tilde{\chi}$ is the scalar dissipation rate, $\tilde{\varepsilon}$ is the turbulent kinetic energy dissipation rate, and u' is a measure of the subfilter RMS velocity fluctuation. The subfilter variance scales with filter width according to the simple relation

$$\widetilde{Z''^2} \propto \Delta^{2/3}. \tag{14}$$

It can be assumed that $\tilde{Z}(1-\tilde{Z})$ does not change with filter width without losing generality. Then the fraction of unresolved scalar energy scales with filter width as

$$\epsilon \propto \Delta^{2/3}. \tag{15}$$

Using the above relation, the refinement criteria can be given as

$$\frac{\epsilon^{n+1}}{\epsilon^n} = \left(\frac{\Delta^{n+1}}{\Delta^n}\right)^{2/3}, \tag{16}$$

where n denotes the refinement level. The above relation is used to refine the grid such that the fraction of unresolved scalar energy compared with the maximum unresolved energy is less than 20%. Based on this, the grid refinement condition can be rewritten as

$$\left(\frac{\Delta^{n+1}}{\Delta^n}\right)^{2/3} = 0.2\frac{\tilde{Z}(1-\tilde{Z})}{\widetilde{Z''^2}}. \tag{17}$$

After the grid is refined, the LES simulation is continued for another 100 steps and the variance field computed again. The above-described RFRP is repeated until either the fractional unresolved energy is globally less than the tolerance level or the maximum grid points that can be handled has been reached. To take care of regions with pure fuel or pure oxidizer, the fractional energy criterion was applied only for mixture fraction values in the range ϵ to $1-\epsilon$, where ϵ was set arbitrarily to 10^{-4}. In addition, when the subfilter variance drops below 1% of the maximum resolvable energy, the computational cell is excluded from the refinement procedure. In the present study, the axial refinement is carried out through conventional techniques by making an educated guess about the flow profile a priori. The radial gradients are more important in the resolution of the shear layer and the refinement strategy is applied for this purpose. In this study, the number of control volumes in the radial direction of the initial grid is set to be the final maximum allowed value. Fig. 1 shows the radial profiles of the fractional energy resolved at two different axial locations for three different grid refinement. It can be observed that the fractional energy resolved increases as the grid is refined around regions of large scalar gradients. However, beyond a particular stage, the fractional energy plot does not seem to change much. The refinement procedure was stopped at this point and the final grid was used to

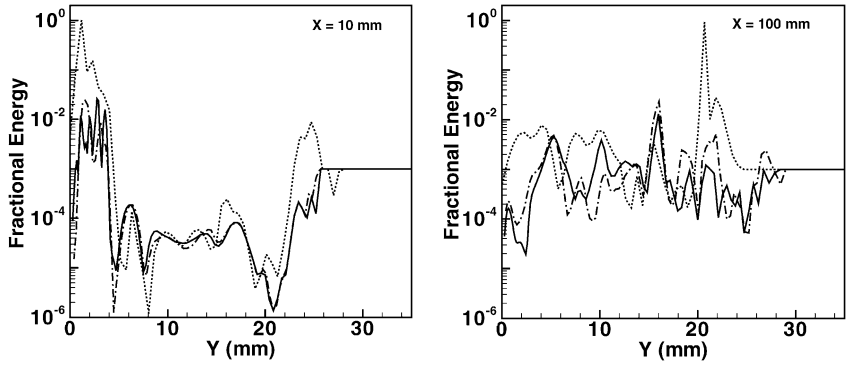

Fig. 1. Radial profiles of the fractional energy resolved at two different axial locations. The dotted line corresponds to the initial grid, the solid line corresponds to the final grid, and the dashed-dotted line represents an intermediate refinement level. The same number of control volumes is used in each case.

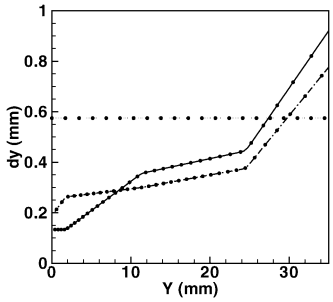

Fig. 2. Radial grid spacing plotted as a function of the radial location for three different refined grids. The dotted line corresponds to the initial grid, the solid line corresponds to the final grid, and the dashed-dotted line represents an intermediate refinement level. The same number of control volumes is used in each case.

simulate the flame. Although these limits were chosen manually in this work, an adaptive mesh refinement strategy can be formulated that adapts the grid based on above-mentioned constraints. Fig. 2 shows the grid spacing as a function of the radial location and shows that the maximum clustering is centered around the inner and outer shear layers. Not surprisingly, regions of strong scalar gradients near the edges of the bluff body required finer resolution. Further details of the computational mesh are provided later.

3. Numerical solution

The Favre-filtered momentum equations as well as the scalar transport equation are solved using a finite-volume scheme in cylindrical coordinates. The momentum equations are discretized using a second-order energy conserving scheme and solved through a fractional-time stepping scheme [25]. The time advancement is implemented using an Adams–Bashforth predictor–corrector algorithm with second-order accuracy. The scalar transport equation is solved using the QUICK scheme [34] with semi-implicit discretization in radial and azimuthal directions. The central difference-based spatial discretization is upwind biased to prevent the formation of wiggle instabilities [35]. The semi-implicit scheme ensures that the time step is not limited by the strong gradients in the radial direction. The eddy viscosity and diffusivity are determined using dynamic models [23,36].

The flamelet equations are solved *a priori* using the FlameMaster code [37]. The GRI-2.11 mechanism [38] was used to obtain the flamelet table. The flamelet table was discretized using 100 points in each of the mean mixture fraction, mixture fraction variance, and scalar dissipation rate spaces. A beta function is used to describe the subfilter mixture fraction PDF, and a log-normal function parameterized by the mixture fraction and filtered scalar dissipation rate was used to describe the subfilter scalar dissipation rate PDF [39]. The filtered scalar dissipation rate is tabulated over the range 0–780 s^{-1}. This range is sufficiently large to include all $\tilde{\chi}$ values that occur in the domain. The flamelet table contains the Favre-filtered density as well as species composition and temperature values. Both molecular viscosity and diffusivity are obtained from mixture properties and are stored in the flamelet table.

The time-stepping scheme contains subiterations of the predictor–corrector nature that advance the momentum and scalar equations. At each subiteration, the scalar transport equation is first advanced to get a better estimate of the density [36]. The new density at this iteration is then used to advance the momentum equations. The continuity equation is enforced subsequently by solving a Poisson equation with source terms obtained in the form of rate of change of error in the mass balance. The Poisson equation is solved using a SOR (successive overrelaxation) scheme that reduces the error to less than 10^{-4}. Numerical tests

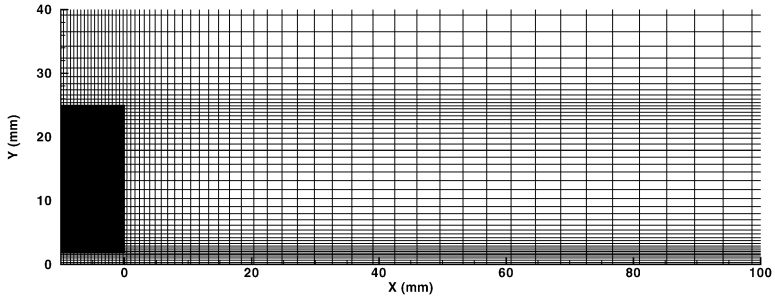

Fig. 3. Computational mesh used in the simulations. The black region represents the bluff body and the domain extends to an upstream location of −10 mm. Every third point in each direction has been plotted. The azimuthal direction is uniformly discretized.

confirm that more stringent error tolerance did not alter the final solution substantially.

4. Simulation conditions

The Sydney experimental configuration consists of a fuel jet of diameter 3.6 mm that is surrounded by a solid bluff body of diameter 50 mm [12]. The unconfined coflow of air is separated from the fuel by the solid body. The fuel consists of a 1:1 methane: hydrogen volume fraction with an approximate stoichiometric ratio of 0.053. Due to some wind tunnel limitations, the experimental statistics for the flow field were obtained at slightly different inlet velocities than the scalar statistics. The simulation domain (Fig. 3) extends from −10 to 360 mm in the axial direction, from 0 to 120 mm in the radial direction, and from 0 to 2π radians in the azimuthal direction. The bluff body is represented by a masked section in the domain and extends from −10 to 0 mm in the axial direction. The domain is resolved by $322 \times 162 \times 66$ control volumes in a cylindrical coordinate system. The jet itself is resolved using 24 control volumes in the radial direction. In addition, a clustered grid is used in the inner and outer shear flow regions to resolve the large velocity gradients. The computational grid was obtained using the RFRP explained earlier.

Two different simulations were carried out corresponding to the flow field and scalar measurements. The first simulation used a fuel jet bulk velocity of 108 m/s and a coflow velocity of 35 m/s. Results from this variable density reacting flow calculations were compared against velocity statistics from the experiment. The second simulation used a slightly higher jet velocity of 118 m/s and a coflow velocity of 40 m/s. Converged scalar statistics from this simulation were compared with scalar profiles from experiment. Initially for both simulations, a cold flow case was simulated using corresponding inlet conditions. Once a statistically stationary solution was obtained, the variable density calculation was initiated.

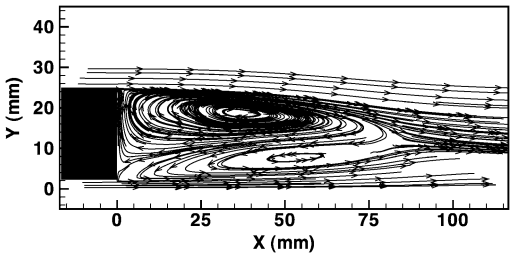

Fig. 4. Streamlines of time-averaged velocity fields from the simulation used to compare with experimental velocity statistics.

The simulations were carried out for several flow-through times calculated on the basis of the coflow jet velocity and the length of the domain. The recursive filter-refinement procedure explained above was used for the first simulation only, and the same grid was reused in the second simulation without further refinement.

Boundary conditions play a crucial role in the predictive capability of the LES. In this particular case, the dynamics of the configuration is determined by the accuracy with which the inner and outer shear layers can be reproduced. The details of the boundary condition and their effect on the flow field are discussed in Section 5.

5. Discussion

5.1. Dynamics of the flow field

Fig. 4 shows the streamlines in the time-averaged velocity profiles near the bluff body. First, the different reaction regions of the system are identified. It is seen that two counter rotating vortices are present in the recirculation region. The main reaction zone, where preheated and partially reacted fuel and oxidizer meet, is located at the end of the two vortices. These vortices transfer enthalpy from the primary reaction zone to the incoming fuel jet and the coflow.

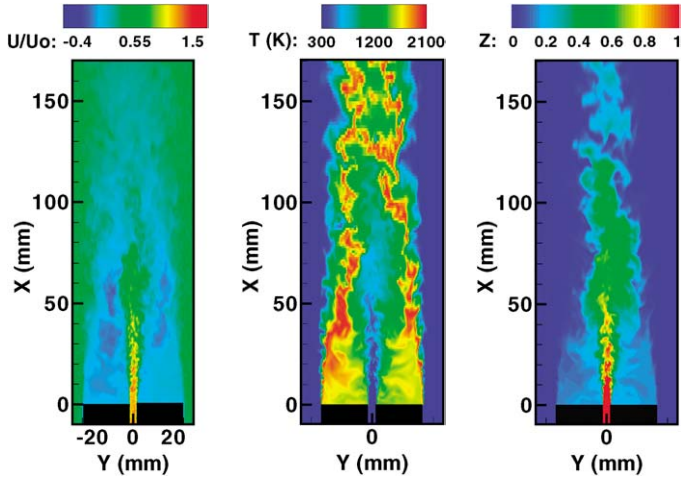

Fig. 5. Two-dimensional contour plots of instantaneous fields from the LES computation: (left) velocity, (middle) temperature, and (right) mixture fraction. U_0 is the bulk velocity of the fuel jet at the inlet.

The low stoichiometric mixture fraction of the fuel mixture helps to establish a thin reaction zone in the outer shear layer between the coflow and the outer vortex. The inner vortex is characterized by mixture fractions higher than the stoichiometric compositions, and hence, lower temperatures and reaction rates. The recirculation zone exhibits large-scale recirculation with the volume of fluid entrapped in either of the vortices changing with time. The large density gradient in the outer shear layer also leads to some amount of vortex shedding. The flow structures are highly three dimensional, with large variations in local compositions along the azimuthal direction. Fig. 5 shows the instantaneous plot of the mixture fraction and the corresponding temperature profile. These snapshots give an idea of the extent of turbulent fluctuations and their interaction with reaction. The velocity contour plot shows the presence of the recirculation zone. The mixture fraction plot clearly indicates the penetration distance of the fuel jet. It can be noted in the temperature plot as well, where the recirculation zone contains large-scale structures and the width of the recirculation zone contracts as the fluid moves away from the bluff body. The structure of the jet is highly unsteady, with jet penetrations varying by as much as 40 mm. On the other hand, the high-temperature region near the bluff body exhibits large-scale recirculation with time scales much larger than those of the axial penetration fluctuations of the jet. This signifies the complexity of this flow and the need to use time-resolved unsteady flow solvers.

5.2. *Effect of boundary conditions on recirculation*

Boundary conditions used for the inner jet as well as the coflow were found to affect the flow field predictions significantly. Typically for the inner jet, LES simulations use inflow profiles computed using a separate LES of a periodic pipe flow. Planes of velocity fields at the outlet of this pipe with the same diameter and Reynolds number as the fuel jet are stored in a file. To obtain a realistic inlet condition, the flow profiles for several thousand time steps are stored and used as input for the actual reacting LES computation. In the first simulation, this procedure is used for the inner fuel jet while the coflow is assumed to have a power law profile,

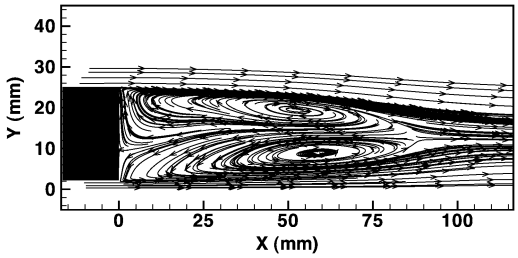

Fig. 6. Streamlines of time-averaged velocity fields from the simulation performed using the power law profile for the coflow inlet velocity.

$$U_{\text{coflow}} = cU_{\text{bulk}}(1 - r_{\text{n}})^p, \tag{18}$$

where U_{bulk} is the coflow bulk velocity; r_{n} is a normalized distance with $r_{\text{n}} = 0$ at the outer edge of the bluff-body and $r_{\text{n}} = 1$ at $Y = 70$ mm; c is a normalization constant that corrects the mass flow; and p is an exponent that controls the shape of the profile. Initially p was set to $1/7$ and c adjusted accordingly. The turbulence intensity was assumed to be uniform in the coflow and was imposed by adding uniform random numbers with mean set to the turbulence intensity. For the first run, this parameter was set to zero

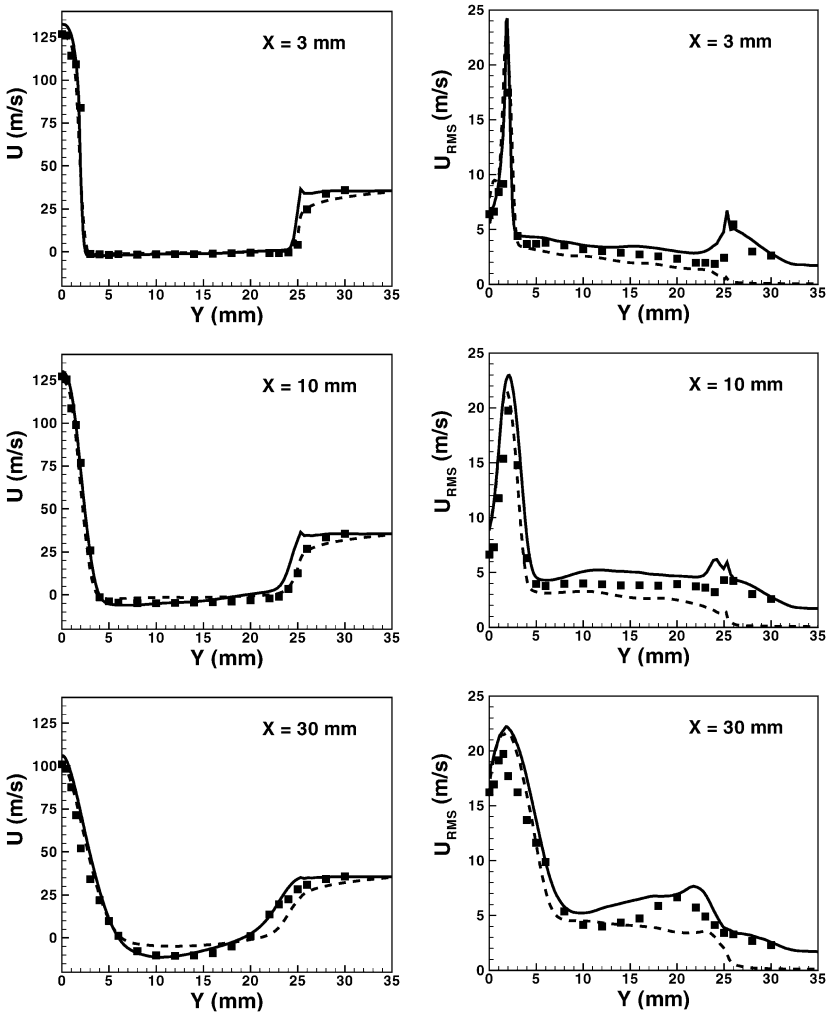

Fig. 7. Comparison of axial mean and RMS velocity fields obtained using two different boundary conditions for the LES simulation and experimental data. Symbols denote experimental data; dashed lines, simulation results with power law profile-based coflow boundary condition; and solid lines, simulation results with boundary conditions based on experimental data.

at $X = -3.5$ mm (upstream boundary). It was found that this inlet condition led to an underprediction of the turbulence in the outer shear layer. The turbulence intensity was then progressively increased but was found to provide no additional improvement in the turbulence predictions. The flow profile was then changed by changing the power law, but again, no substantial improvement occurred.

To overcome this problem, a new approach was followed. The experimental data also provide the inflow conditions at $X = 0$ mm. Because the simulation domain extends upstream, an extrapolation procedure is necessary. Based on the inflow velocity profiles from the experiment, a linear estimate of the boundary conditions upstream was calculated. Based on a similar estimate, the RMS velocity profile was extrapolated as well. To produce a turbulent inflow condition, a random noise term was added to the mean velocity profile,

$$U_{\text{coflow}}(y,t) = \langle U\rangle(y) + \langle U_{\text{rms}}\rangle(y)\xi, \tag{19}$$

where $\langle U\rangle(y)$ and $\langle U_{\text{rms}}\rangle(y)$ are estimates of the inlet profile based on the experimental inlet conditions, and ξ is a uniform random number. Further analysis of the fuel jet inflow conditions revealed that the turbulent pipe flow data led to a faster decay of the centerline jet velocity. Based on similar linear estimates, the inlet jet velocity was corrected such that the mean centerline velocity at the first measurement station matches the experimental data to within reasonable accuracy.

This procedure was found to appreciably increase the accuracy of the simulations. The first indicator of the differences in the simulations is the location of

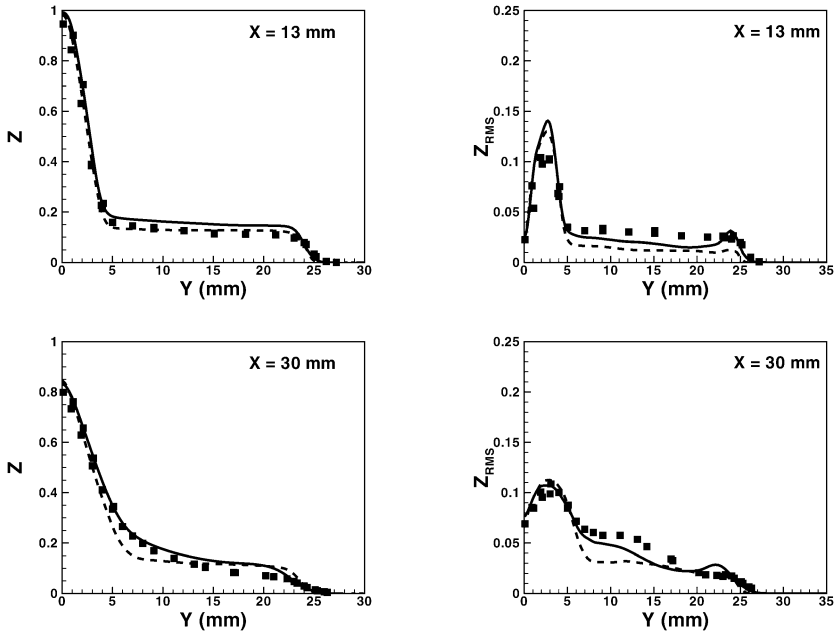

Fig. 8. Comparison of mean and RMS mixture fraction fields obtained using two different boundary conditions for the LES simulation and experimental data. Symbols denote experimental data; dashed lines, simulation results with power law profile-based coflow boundary condition; and solid lines, simulation results with boundary conditions based on experimental data.

the recirculation vortices in the streamline plots of the mean velocity profiles. Fig. 4 shows the simulation results obtained using the improved boundary conditions. Fig. 6 shows the streamline plots obtained using the boundary conditions corresponding to Eq. (18). It is clear that improved boundary conditions move the outer vortex closer to the bluff body. In addition, the outer vortex has increased strength near the bluff-body. The effect of this change in the location of the vortical structures can be observed in the mean profiles. Fig. 7 shows radial profiles of mean axial velocity and RMS axial velocity at three axial locations close to the bluff body. Both simulations predict the mean profiles quite accurately. It can be seen that the simulation with the improved boundary conditions better predicts the RMS velocity profile close to the bluff body. This is a direct consequence of the stronger recirculation zone near the bluff body. In addition, it is observed (at $X = 30$ mm) that the width of the recirculation region is correctly predicted using the improved boundary conditions. Consequently, the mixture fraction field (Fig. 8) is predicted better using the improved boundary conditions. At both axial locations considered, the RMS mixture fraction shows quantitatively better results and qualitatively matches the behavior the experimental configuration. With the original power law profile-based simulation, the RMS mixture fraction closest to the bluff body is underpredicted, which further confirms the weak large-scale recirculation predicted by the simulation.

In summary, the improved boundary conditions that try to match the experimental boundary conditions capture the flame physics quite accurately. In later sections, it is shown that a highly accurate mixture fraction field is predicted as well, dispelling notions that the accurate prediction of the flow field invariably leads to an underprediction of the flame height [18].

5.3. Velocity statistics

The velocity statistics for a fuel jet velocity of 108 m/s and coflow velocity of 35 m/s were compared. The reacting flow simulation was run for six residence times calculated on the basis of the inlet coflow velocity and the length of the computational domain. The boundary conditions are based on the experimental data as explained in the previous section.

Fig. 9 compares simulation results with experimental radial profiles of velocity components at four different axial locations. The simulation predicts the velocity quite accurately. In the near-inflow region, the decay of the fuel jet velocity is predicted quite well, indicating that the grid is sufficiently resolved in this region. At all locations considered, the width of the recirculation region is predicted well, indicating that the essential dynamics of the flame are captured. Axial velocities are slightly underpredicted at $X = 70$ mm and further downstream. Similar behav-

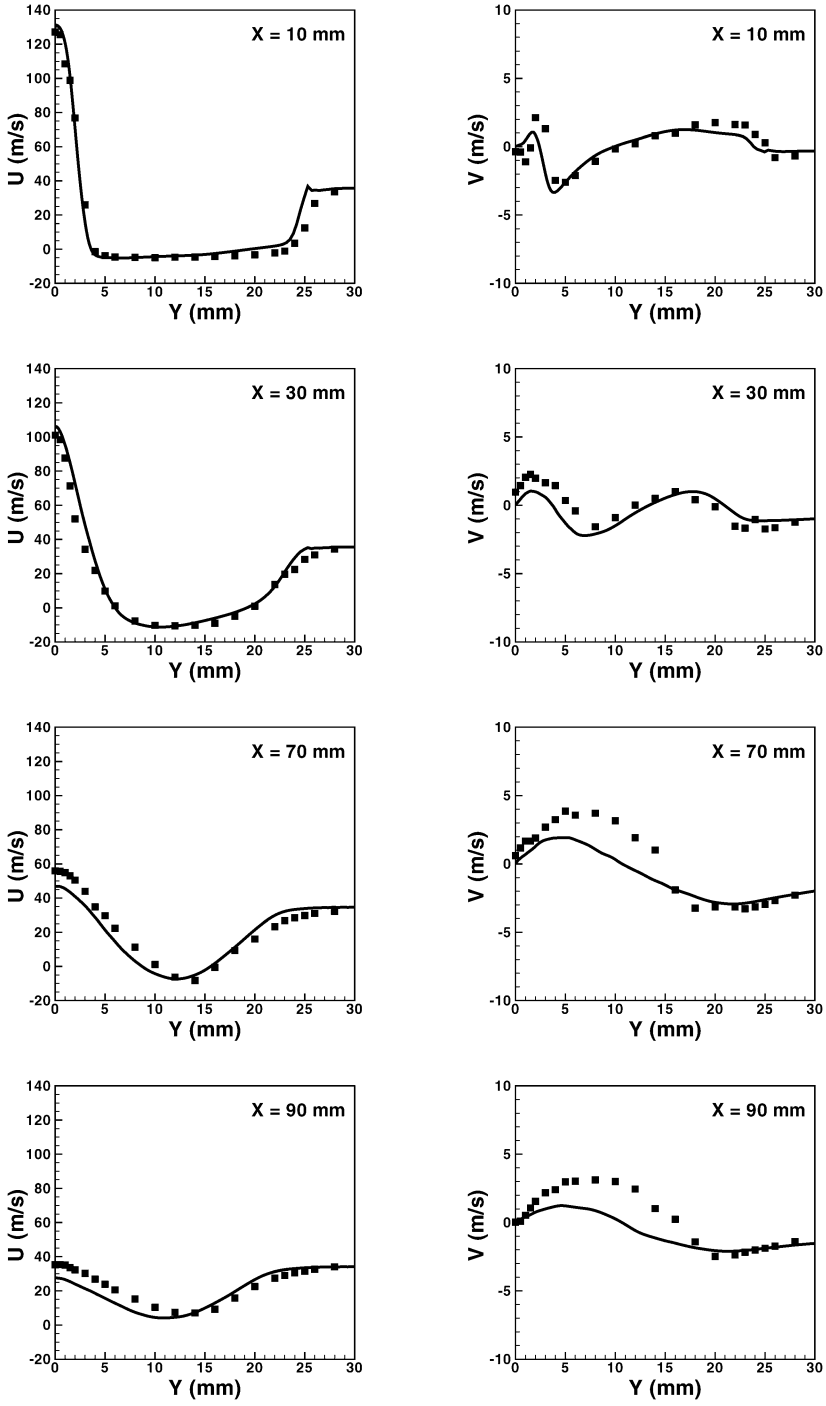

Fig. 9. Comparison of axial (left) and radial (right) velocity with experimental data at different axial locations. From top to bottom, $X = 10$, 30, 70, and 90 mm. Symbols represent experimental data, and lines, simulation results.

ior is noted for the radial velocities. The predictions are quite accurate in the recirculation region, while the peaks in the velocity profiles are underpredicted in the downstream locations. It has been noted that there are significant experimental discrepancies at downstream locations [16]. Taking this into account, the current predictions are able to capture the flame structure and the essential characteristics of the flow.

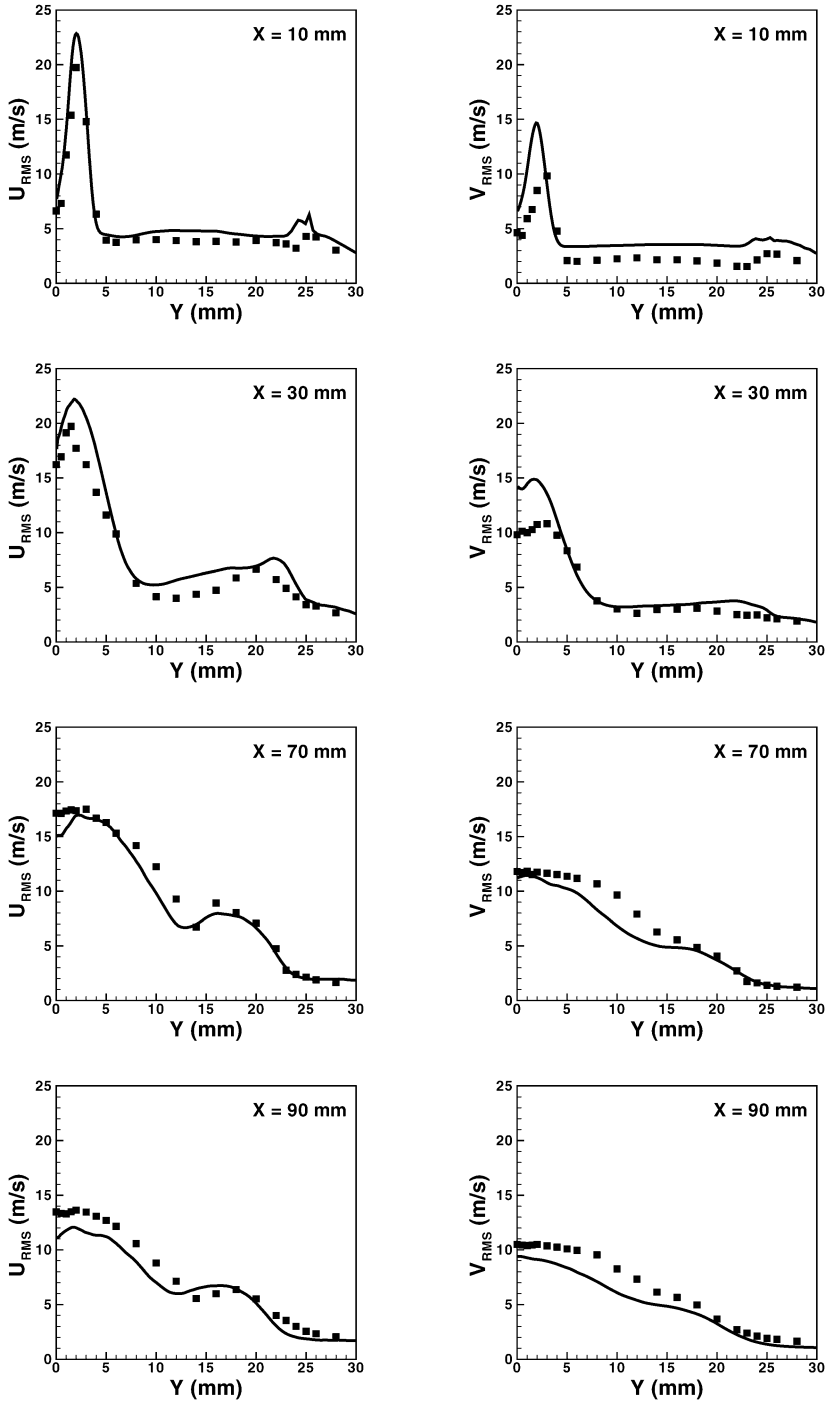

Fig. 10. Comparison of RMS of axial (left) and radial (right) velocity fluctuations with experimental data at different axial locations. From top to bottom, $X = 10$, 30, 70, and 90 mm. Symbols represent experimental data, and lines, simulation results.

Although some differences between simulations and experiments have been noted, the species profiles to be discussed later show very good agreement with experimental data.

Fig. 10 shows radial profiles of time-averaged velocity fluctuations at different axial locations. The near-inflow locations show good agreement with the experimental data for both components. The peak in

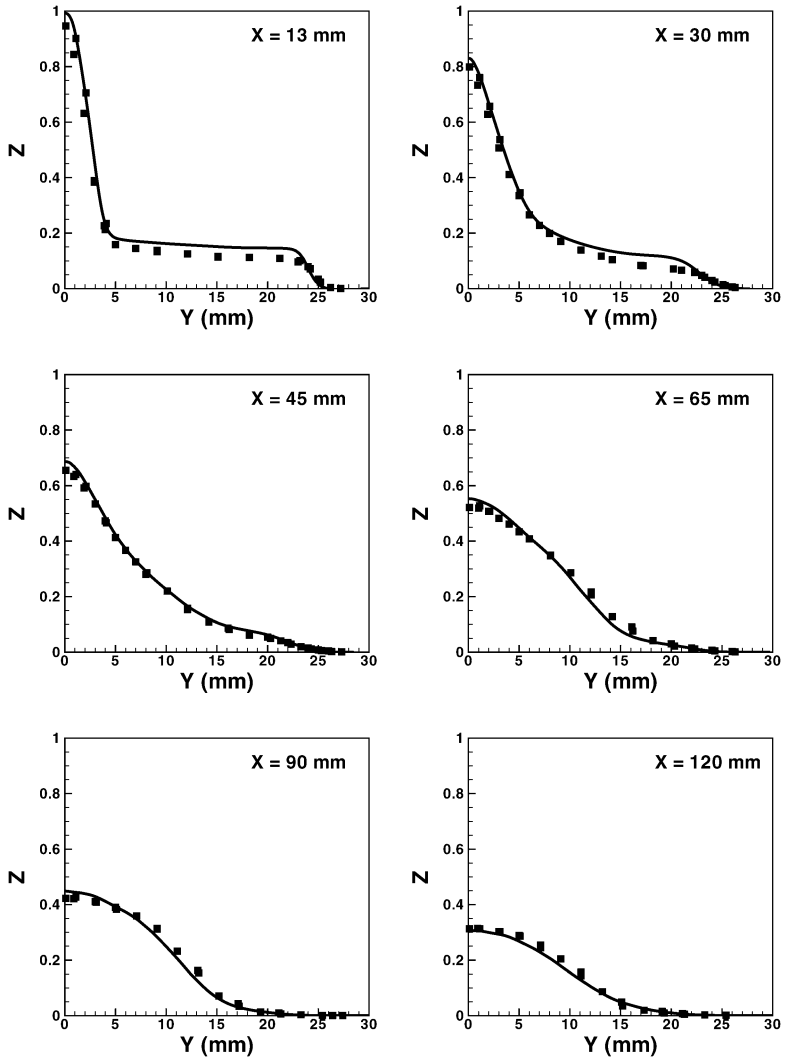

Fig. 11. Comparison of mixture fraction profiles with experimental data at different axial locations. Symbols represent experimental data, and lines, simulation results.

the axial fluctuations is captured accurately, reinforcing that the grid resolution in the fuel jet region is able to capture the magnitude of the shear. Due to the improved boundary conditions, the velocity fluctuations in the recirculation region are captured very accurately. It is seen that both the axial and radial fluctuations show a small peak near the outer edge of the bluff body corresponding to the interaction of the coflow with the recirculating fluid. Further downstream, this secondary peak in the RMS axial velocity profile moves toward the centerline, indicating that the width of the recirculation zone decreases with axial distance. At all axial locations shown, the simulation results exhibit very good agreement with experimental data. Detailed comparisons with the entire experimental data at other axial locations have been carried out (not shown here) and similar good accuracy is seen. From these comparisons, it is readily seen that the LES simulations capture the complex flow patterns in a bluff-body-stabilized flow and provide predictions in good agreement with experimental data.

5.4. Species statistics

The experimental data for the species statistics were collected using an inlet jet velocity of 118 m/s and a coflow velocity of 40 m/s. This is considered to have the same blowout characteristics as the experimental setup used for the velocity statistics [12].

Fig. 11 shows the radial profiles of mixture fraction at different axial locations. The agreement is

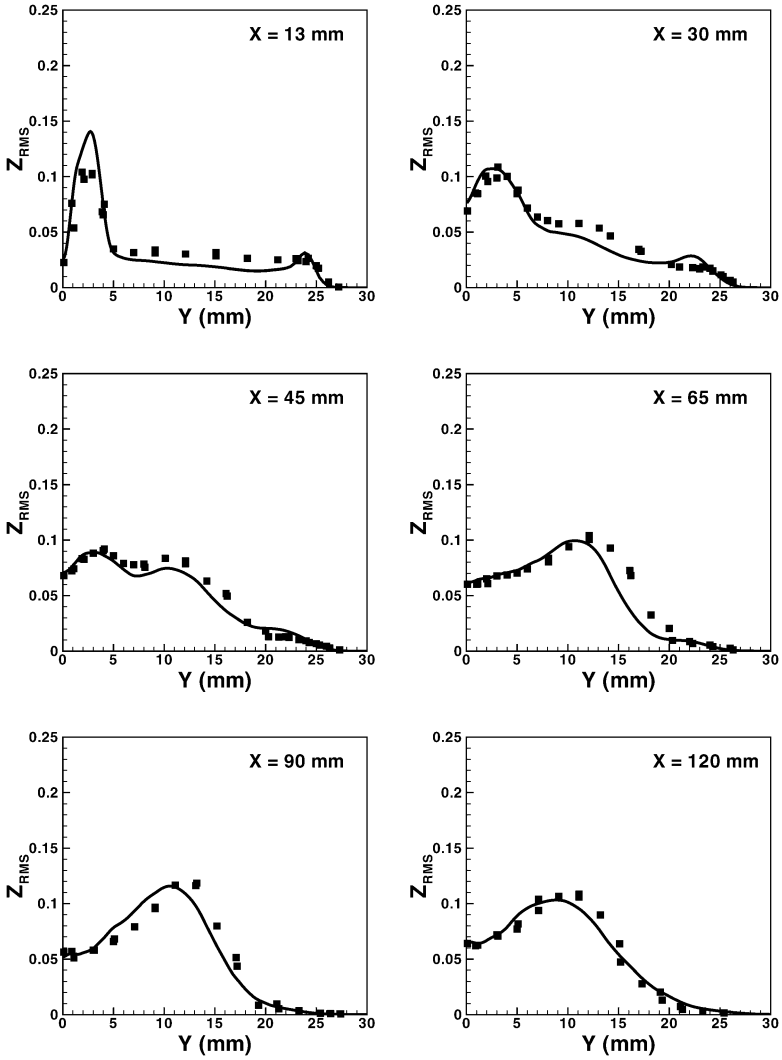

Fig. 12. Comparison of profiles of RMS mixture fraction fluctuations with experimental data at different axial locations. Symbols represent experimental data, and lines, simulation results.

excellent at all considered locations. The LES computation accurately predicts the decay of the fuel jet even at the last downstream position considered. It is emphasized that to the knowledge of the authors, no other simulation result has so far predicted the mixture fraction field with this accuracy at downstream locations [18]. The RMS mixture fraction profiles at different axial locations are plotted in Fig. 12. As explained before, the improved boundary conditions dramatically increase the accuracy of the mixing field predictions. It can be observed that near the bluff body, the strong recirculation leads to large-scale mixing that has been captured well in the RMS mixture fraction plot (Fig. 12). Again, the shear layer between the coflow and the recirculation zone leads to a secondary spike in the RMS profile, similar to that observed in the RMS velocity plots. The profiles further downstream show excellent agreement except at $X = 65$ mm, where there seems to be slight underprediction of the mixture fraction fluctuations in the outer shear layer. This level of accuracy in temporal statistics provides an excellent starting point for analyzing the interaction of chemistry and turbulent transport of the scalars.

Fig. 13 shows radial profiles of temperature at different axial locations. The temperature profile shows a peak near the outer shear layer at $X = 13$ mm. Even though the mean mixture fraction and RMS mixture fraction profiles are predicted with reasonable accuracy, the temperature profile indicates enhanced reactions at the interface of the recirculation and coflow zones. This could indicate either that the

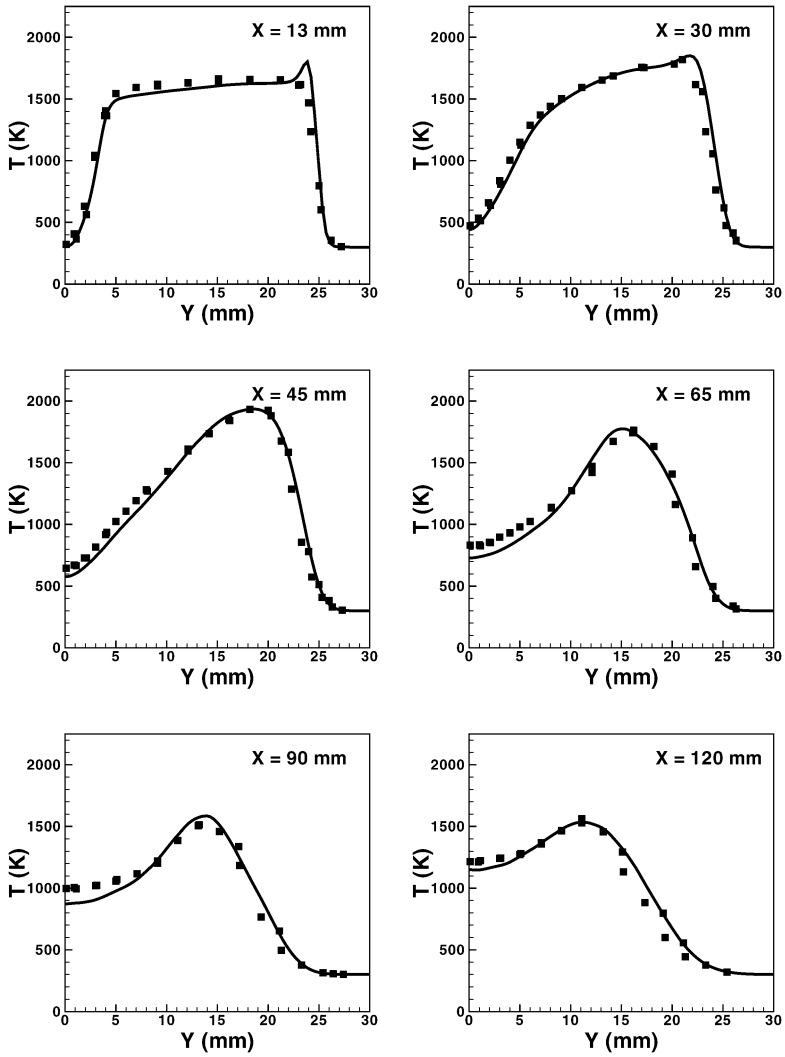

Fig. 13. Comparison of temperature profiles with experimental data at different axial locations. Symbols represent experimental data, and lines, simulation results.

flamelet assumptions are not strictly valid in this zone or that the subfilter variance is being underpredicted. The validity of the flamelet assumption can be tested only through a separate finite chemistry-based solution methodology and is concurrently being pursued. Though the recursive refinement strategy decreases the influence of the subfilter variance model, it is infeasible to completely eliminate the model influence. As pointed out by a reviewer, the finite probe volumes used in the measurements could also account for some of the errors. In any case, due to the lack of sufficient evidence, it is not possible to point to the exact source of this discrepancy. Further downstream, the temperature profiles are reproduced quite accurately. Beyond $X = 45$ mm, the mean temperature is underpredicted at the centerline. This is significant, as the mixture fraction profiles are quite accurately predicted. These differences in mean temperature point to extreme sensitivity of the species evolution to local subfilter models or a possible deviation from flamelet regime. Overall, the mean temperature predictions agree well with experimental data.

The species profiles are compared with experimental data in Figs. 14–16. The CO_2 profiles show good agreement for all axial positions considered. It is observed that the profiles follow the temperature predictions up to $X = 90$ mm. At further downstream locations, interestingly, the trends are reversed near the centerline. Any underprediction in temperature leads to an overprediction in the CO_2 profiles. This indicates a possible change in the reaction mechanism controlling CO_2 production. The CO profiles

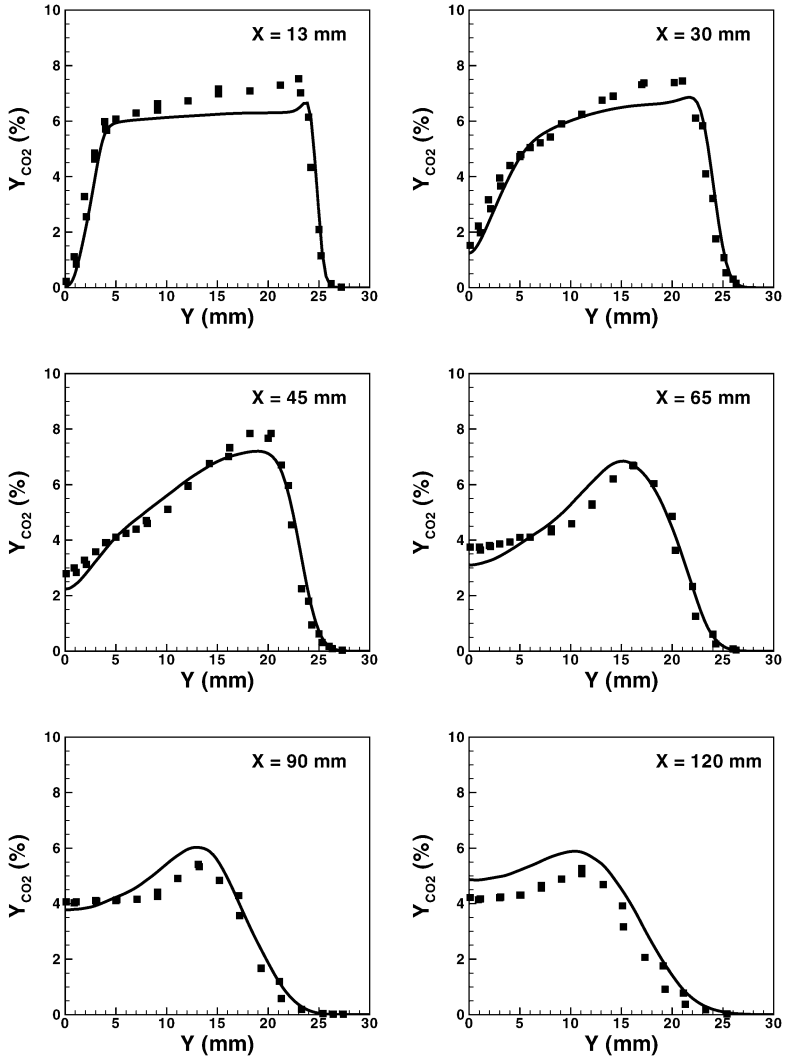

Fig. 14. Comparison of CO_2 mass fraction profiles with experimental data at different axial locations. Symbols represent experimental data, and lines, simulation results.

show similar results, with a reversal of trends at $X = 65$ mm. At all locations considered, the errors in the predictions are very small considering the experimental uncertainties. At downstream locations, there is a slight overprediction of the CO mass fraction at the centerline. The H_2O profiles demonstrate very good agreement at all axial stations shown and no further discussion is necessary.

Fig. 17 shows the radial profile of the hydroxyl radical. At the axial location nearest to the bluff body, the agreement is not good. The OH radical is underpredicted in the recirculation region and is overpredicted in the outer shear layer. Despite the the excellent agreement of mixture fraction and RMS mixture fraction profiles with experimental data, the OH concentration is poorly reproduced. This indicates a possible departure from the flamelet regime. In addition, modeling errors in scalar dissipation, as well as subfilter variance, can also lead to substantial errors. This can be explained by analyzing the flamelet solution at any given mean mixture fraction as a function of the mixture fraction variance (Fig. 18). It can be seen that the OH profile is a highly nonlinear function of the subfilter variance, implying that minor errors in model predictions can lead to large deviations of the OH profile. The dynamic model [30] is known to underpredict the scalar variance [28], which could lead to increased reactions rates and, consequently, a higher hydroxyl value.

From the above discussion, it can be concluded that the flamelet model is able to capture the trends in the profiles of the species. As far as major species like

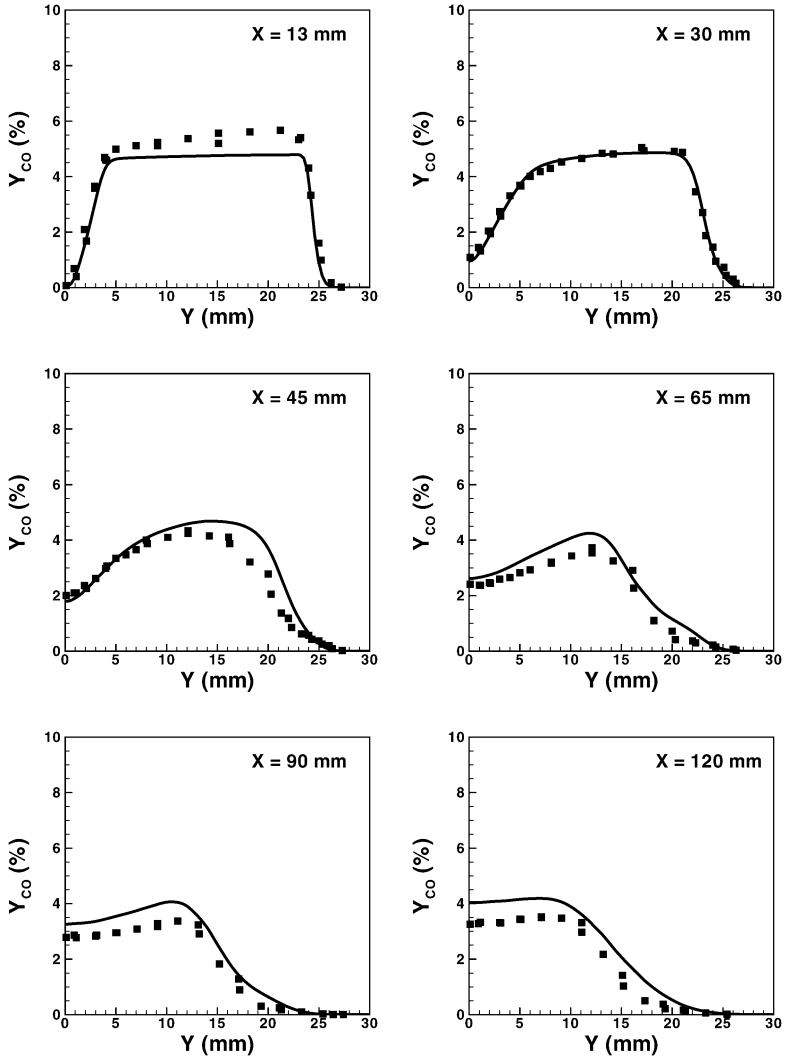

Fig. 15. Comparison of CO mass fraction profiles with experimental data at different axial locations. Symbols represent experimental data, and lines, simulation results.

CO_2 are concerned, the predictions are quite accurate. It is noted here that the experimental errors should also be taken into account. Minor species like CO and OH show some distinct trends in the deviations from experimental data. These discrepancies may indicate a deviation from flamelet regime or a cumulative effect of the subfilter modeling errors. In general, the LES method combined with the RFRP and a simple chemistry model is able to provide a very good reproduction of the experimental data.

6. Conclusions

A recursive filter-refinement-based LES simulation of a bluff-body-stabilized flame has been conducted. A laminar flamelet model was used to describe the thermochemistry. Improved boundary conditions were implemented to reproduce the turbulence levels in the outer shear layer. Through two simulations employing two different boundary conditions, it was shown that the accurate prediction of the turbulence levels in the outer shear layer is critical in accurate prediction of the RMS velocity profiles as well as RMS mixture fraction profiles. By comparing stream traces, the effect of the outer shear layer on the flow structure was discussed. The results based on the improved boundary condition were used for further analysis.

Both velocity and species statistics have been compared with experimental data. The velocity profiles show excellent agreement with experimental data

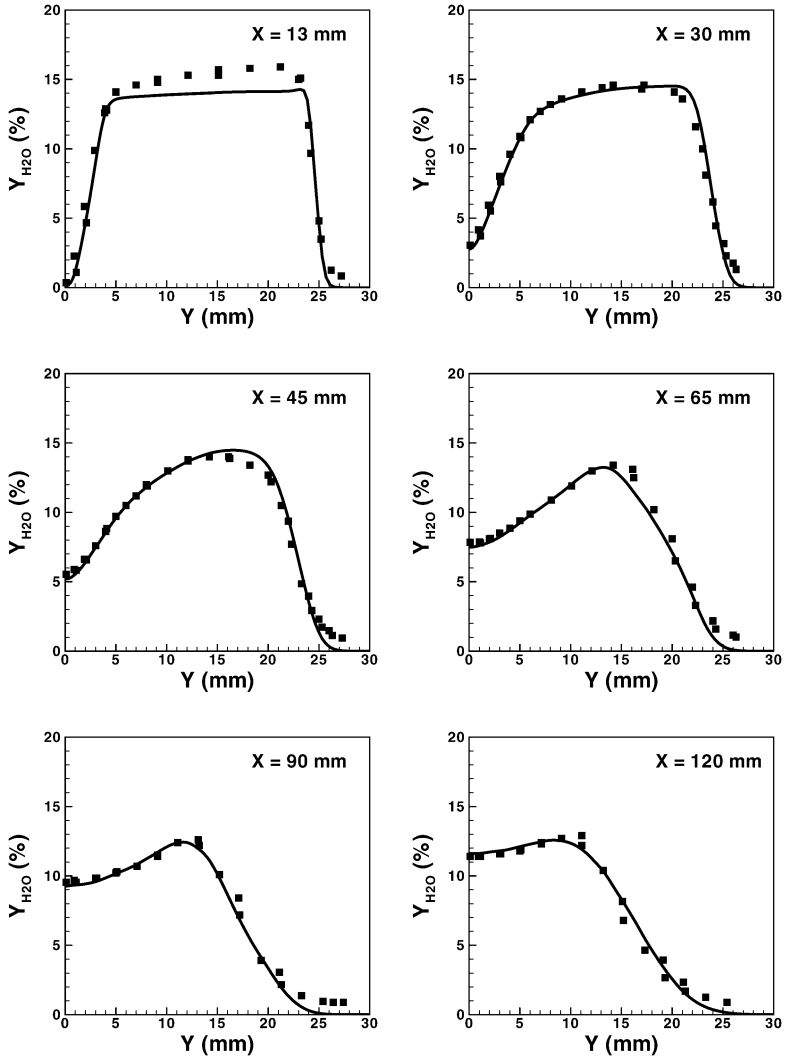

Fig. 16. Comparison of H_2O mass fraction profiles with experimental data at different axial locations. Symbols represent experimental data, and lines, simulation results.

for mean and RMS quantities of both the axial and radial velocity components. The mixture fraction profiles have been shown to be accurately captured by the LES solver. The time-averaged mixture fraction fluctuations show very good agreement at all axial locations. In general, the species profiles are in good agreement with experimental data, indicating that the laminar flamelet assumption provides a good basis for simulating such flames. Only profiles of the hydroxyl radical showed significant differences from the experimental data. From the LES simulations, it can be concluded that current reaction models are able to describe flame physics reasonably well. Considering the complexity of the flow, the simulations are able to predict quantitatively most of the experimental profiles. It is concluded that if large-scale mixing quantified by mean and RMS mixture fraction profiles is accurately predicted, both species and velocity profiles can be obtained within reasonable accuracy. A comparison with previous simulations using RANS demonstrates significantly improved results using LES, even with simple combustion models. This can be attributed to improved predictions of the scalar mixing process.

The improved boundary conditions used here underline the sensitivity of the LES technique. By varying the inlet conditions of the coflow, it was possible to understand the role of the outer shear layer in determining the structure of the flame. The mixing field comparison showed that accurate prediction of velocity field does not automatically preclude good agreement of the mixture fraction profiles with experimental data. Almost all simulations reported so far

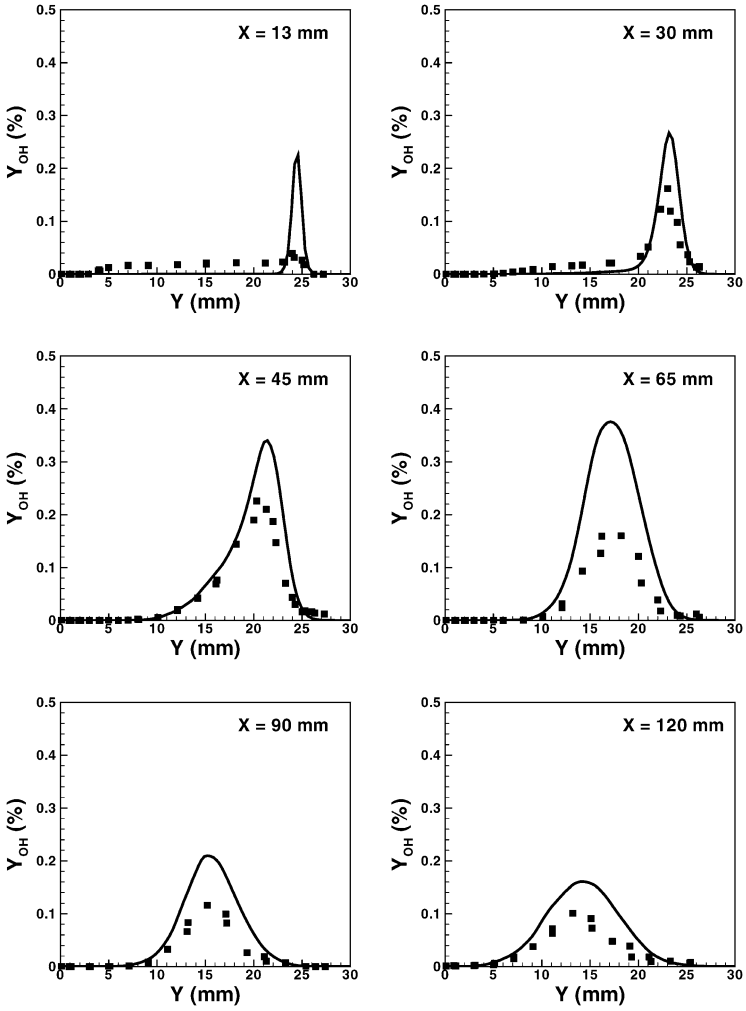

Fig. 17. Comparison of OH mass fraction profiles with experimental data at different axial locations. Symbols represent experimental data, and lines, simulation results.

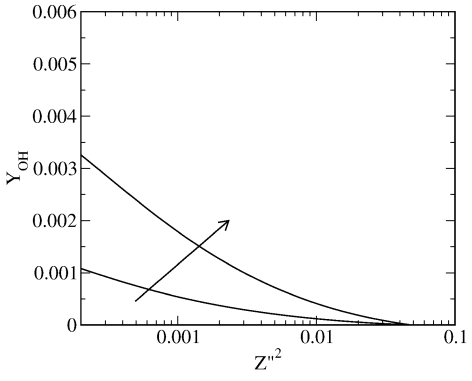

Fig. 18. Mass fraction of OH radical as a function of subfilter mixture fraction variance at the maximum and minimum scalar dissipation rates tabulated in the look-up table. The higher peak corresponds to the larger dissipation rate.

have failed to predict the downstream mixing field. The construction of an optimal grid seems to be an important step in increasing the predictive capability of LES. This study shows that a highly resolved grid for the central jet is required to predict downstream mixing fields. In addition, the three-dimensional nature of the jet needs to be taken into account through sufficient grid resolution in the azimuthal direction.

As mentioned earlier, the LES scheme does not resolve the reaction length scales. However, through the choice of a reaction model with sufficiently detailed modeling, flows with such complexity can be predicted quite accurately. This clearly shows that an accurate prediction of large-scale mixing is critical in understanding turbulent flames. By choosing an appropriately refined grid, the effect of subfilter scalar fluctuations can be minimized increasing the validity of the LES computations. The RFRP used

here is shown to yield excellent results, indicating that such a strategy should be explored further. In the future, an automated algorithm will be formulated to adapt grids to flow conditions. This is in stark contrast to Reynolds averaging-based approaches, where a subgrid model is critical in making quantitative predictions and is thus subject to errors from modeling assumptions. Use of dynamic models in LES for subfilter terms further increases the fidelity and accuracy of the computations. It is concluded that the current LES models for flow and chemistry combined with an appropriately refined computational mesh can be used to obtain quantitative predictions of complex reacting flows.

References

[1] R.O. Fox, Rev. Inst. Fr. Petrole 51 (1996) 215.
[2] R.O. Fox, Computational Models for Turbulent Reacting Flows, Cambridge Univ. Press, London/New York, 2003.
[3] H. Pitsch, H. Steiner, Phys. Fluids 12 (2000) 2541–2554.
[4] J.H. Ferziger, M. Peric, Computational Methods for Fluid Dynamics, third ed., Springer-Verlag, Berlin/New York, 2002.
[5] S.B. Pope, Combust. Flame 27 (1976) 299–312.
[6] N. Peters, Turbulent Combustion, Cambridge Univ. Press, London/New York, 2000.
[7] R.W. Bilger, Phys. Fluids 5 (1993) 436–444.
[8] A.Y. Klimenko, Phys. Fluids 7 (1995) 446–448.
[9] A.Y. Klimenko, S.B. Pope, Phys. Fluids 15 (2003) 1907–1925.
[10] H. Pitsch, Proc. Combust. Inst. 29 (2003) 1971–1978.
[11] F.D. Mare, W.P. Jones, K.R. Menzies, Combust. Flame 137 (2004) 278–294.
[12] B.B. Dally, A.R. Masri, R.S. Barlow, G.J. Fietchner, Combust. Flame 114 (1998) 119–148.
[13] S.H. Kim, K.Y. Huh, Combust. Flame 130 (2002) 94–111.
[14] B. Merci, D. Roekaerts, T.W.J. Peeters, E. Dick, in: Proceedings of the Fifth International Workshop on Measurement and Computation of Turbulent Non-premixed Flames, Delft, The Netherlands, 2000, pp. 226–227.
[15] Sixth International Workshop on Measurement and Computation of Turbulent Non-premixed Flames, 2002, http://www.ca.sandia.gov/tnf/abstract.html.
[16] M. Muradoglu, K. Liu, S.B. Pope, Combust. Flame 132 (2003) 115–137.
[17] B.B. Dally, D.F. Fletcher, A.R. Masri, Combust. Theory Modell. 2 (1998) 193–219.
[18] Seventh International Workshop on Measurement and Computation of Turbulent Non-premixed Flames, 2004, http://www.ca.sandia.gov/tnf/abstract.html.
[19] S.B. Pope, Phys. Fluids 6 (1994) 973–985.
[20] J. Smagorinsky, Mon. Weather Rev. 91 (1963) 99–164.
[21] J. Bardina, J.H. Ferziger, W.C. Reynolds, AIAA Paper 80-1357 (1980).
[22] M. Germano, J. Fluid Mech. 286 (1991) 229–255.
[23] P. Moin, K. Squires, W. Cabot, S. Lee, Phys. Fluids A 3 (1991) 2746–2757.
[24] S. Ghosal, T.S. Lund, P. Moin, K. Akselvoll, J. Fluid Mech. 286 (1995) 229–255.
[25] C.D. Pierce, P. Moin, J. Fluid Mech. 504 (2004) 73–97.
[26] V. Eswaran, S.B. Pope, Phys. Fluids 31 (1988) 506.
[27] A. Juneja, S.B. Pope, Phys. Fluids 8 (1996) 2161.
[28] J. Jimenez, A. Linan, M.M. Rogers, F.J. Higuera, J. Fluid Mech. 349 (1997) 149–171.
[29] S.S. Girimaji, Y. Zhou, Phys. Fluids 8 (1996) 1224–1236.
[30] C.D. Pierce, P. Moin, Phys. Fluids 10 (1998) 3041–3044.
[31] C. Jimenez, F. Ducros, B. Cuenot, B. Bedat, Phys. Fluids 13 (2001) 1748.
[32] J.P. Mellado, S. Sarkar, C. Pantano, Phys. Fluids 15 (2003) 3280–3307.
[33] D. Wang, C. Tong, Phys. Fluids 14 (2002) 2170–2185.
[34] B.P. Leonard, Comput. Methods Appl. Mech. 19 (1979) 59–98.
[35] K. Akselvoll, P. Moin, J. Fluid Mech. 315 (1996) 387–411.
[36] C.D. Pierce, Progress-Variable Approach for Large-Eddy Simulation of Turbulence Combustion, Ph.D. thesis, Stanford University, 2001.
[37] H. Pitsch, AC++ Computer Program for 0-D and 1-D Laminar Flame Calculations, RWTH Aachen (1998).
[38] C.T. Bowman, R.K. Hanson, D.F. Davidson, et al., Gri-mech 2.11, 1995, http://www.me.berkeley.edu/gri_mech/.
[39] H. Pitsch, Combust. Flame 123 (2000) 358–374.